

The Constellation-X RGS options: Raytrace Modeling of the Off-plane Gratings

K.A. Flanagan, J.E. Davis, R.K. Heilmann, A.M. Levine, M. McGuirk, G.R. Ricker,
M.L. Schattenburg, M. Wise¹,
A. Rasmussen²,
J. Bookbinder, M. Freeman, T. Gaetz, D. Jerius, D. Nguyen, W. Podgorski, P. Reid³,
W. Cash, A. Shipley⁴,
D. Gallagher, P. Huang, S. Jordan⁵

¹MIT Center for Space Research, Cambridge, MA, USA;

²Columbia University, New York, NY, USA;

³Smithsonian Astrophysical Observatory, Cambridge, MA, USA;

⁴University of Colorado, Boulder, CO, USA;

⁵Ball Aerospace and Technologies Corporation, Boulder, CO, USA

ABSTRACT

The Reflection Grating Spectrometer of the Constellation-X mission has two strong candidate configurations. The first configuration, the in-plane grating (IPG), is a set of reflection gratings similar to those flown on XMM-Newton and has grooves perpendicular to the direction of incident light. In the second configuration, the off-plane grating (OPG), the grooves are closer to being parallel to the incident light, and diffract along a cone. It has advantages of higher packing density, and higher reflectivity. Confinement of these gratings to sub-apertures of the optic allow high spectral resolution. We have developed a raytrace model and analysis technique for the off-plane grating configuration. Initial estimates indicate that first order resolving powers in excess of 1000 (defined with half-energy width) are achievable for sufficiently long wavelengths ($\lambda \gtrsim 12\text{\AA}$), provided separate accommodation is made for gratings in the subaperture region farther from the zeroth order location.

Keywords: Off-plane grating, reflection gratings, diffraction, X-ray, spectrometer, high resolution, CCD

1. INTRODUCTION

Constellation-X is a high-throughput high-resolution spectroscopy mission¹ that is one of NASA's two "Beyond Einstein" great observatories.² Below 10 keV, high-resolution spectral coverage is provided by a reflection grating spectrometer (RGS) and the X-Ray Microcalorimeter System (XMS)³ used with the Soft X-Ray Telescope (SXT).⁴ The wavelength range is extended to 40 keV or more by a set of high-energy mirrors, the Hard X-Ray Telescope (HXT),⁵ and associated detectors.

The Reflection Grating Spectrometer (RGS) of Constellation-X provides high resolution X-ray spectra over 0.25–2.0 keV (6 Å– 50Å). The instrument consists of two components, a grating array and a detector readout system. As illustrated in Figure 1, a Reflection Grating Array (RGA) is located behind the SXT; it reflects and disperses X-rays to the RGS Focal Plane Camera (RFC). The RFC employs two camera systems: The Zero Order Camera (ZOC) captures the X-rays which are reflected into the zeroth order, providing an essential reference for determining wavelength by tracking small aspect drifts. The Spectroscopy Readout Camera (SRC) captures the dispersed X-ray spectrum, providing moderate energy resolution for order sorting. The baseline RFC devices are event-driven X-ray CCDs, in which only those pixels with signal charge are saved and digitized. This allows high speed operation with lower power.⁶

The RGA consists of a large number (~ 1000) of individual gratings held at grazing incidence with respect to the local converging beam from the SXT. The RGA uses a modular approach: ~ 10 identical gratings are

Further author information: (Send correspondence to K.A.F.)

K.A.F.: E-mail: kaf@space.mit.edu, Telephone: 617 258-7324

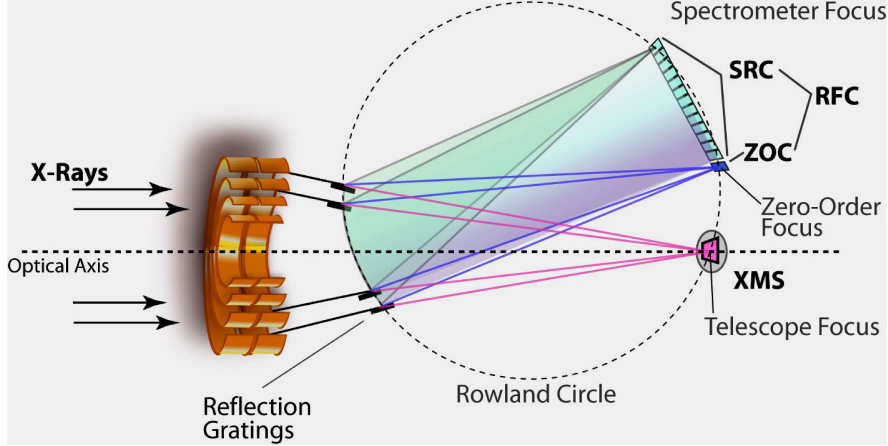


Figure 1. RGS layout. The Reflection Grating Array (RGA) is located behind the SXT mirrors and reflects and disperses X-rays to the RGS Focal Plane Camera (RFC). X-rays which are not intercepted by the gratings are captured by the XMS at the telescope focus. The RFC employs two camera systems: The Zero Order Camera (ZOC) and the Spectroscopy Readout Camera (SRC). The Rowland circle geometry pictured above applies to the in-plane grating configuration.

Table 1. Design parameters for in-plane and off-plane gratings.

Parameter	In-plane	Off-plane
Ruling density $1/d$ (line/mm)	407	5800
Cone half-angle γ (degrees)	90	2.7
Azimuthal incidence angle α (degrees)	88.39	30
Incidence angle ψ_i (degrees)	1.61	
Facet blaze (degrees)	0.605	11

aligned and assembled into grating subassembly modules, as illustrated to the left in Figure 2. These modules are arranged and oriented appropriately behind the SXT.

Two grating configurations are under consideration for the RGA. One of these configurations, the in-plane gratings (IPG), is patterned substantially after the successful XMM-Newton RGS. The second configuration, the off-plane gratings (OPG), may have advantages in spectral resolving power. The purpose of this paper is to present results of a raytrace model of the OPG and give estimates of its spectral resolving power.

1.1. Two Grating Configurations

The “in-plane gratings” (IPG),⁷ employ gold gratings patterned on thin silicon or glass substrates with a ruling density of 407 lines/mm (a grating period of $2.46 \mu\text{m}$), as shown to the right in Figure 2. The gratings are held so that the X-rays are incident at angle 1.61° relative to the plane of the grating; thus, the projected linewidth is much finer, boosting the dispersion proportionately. Each grating is $100\text{mm} \times 200\text{mm}$, and employs a “chirp” or varying period of 5% across the face of the grating. The grating lines are perpendicular to the incident X-rays, and the dispersed ray is in the plane containing the grating normal and the incident ray. (Thus, as the diffraction angle increases, the angle between the diffracted ray and the surface of the grating increases.) Design parameters for the IPG are given in Table 1.

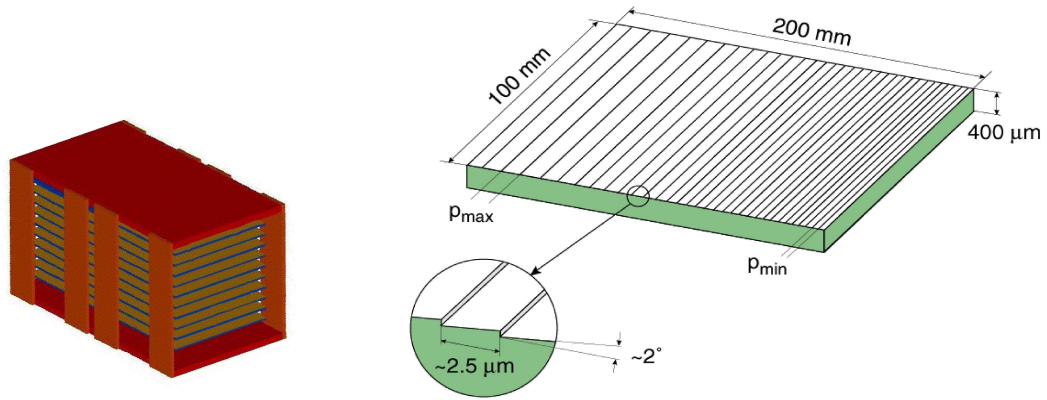


Figure 2. (Left) The gratings are arranged in modules containing ~ 10 identical gratings held at grazing incidence with respect to the converging X-ray beam behind the SXT. Both in-plane and off-plane gratings will use a modular approach. (Right) In-plane gratings will be patterned in gold on thin silicon or glass substrates with a “chirped” (varying) linewidth of relatively coarse ruling density (see Table 1). Each grating will be $100\text{mm} \times 200\text{mm}$ size with a small facet blaze. The off-plane grating will differ from this picture, having a much finer ruling density, radial grooves oriented nearly parallel to the incident beam, with larger facet blaze and possibly thicker substrate.

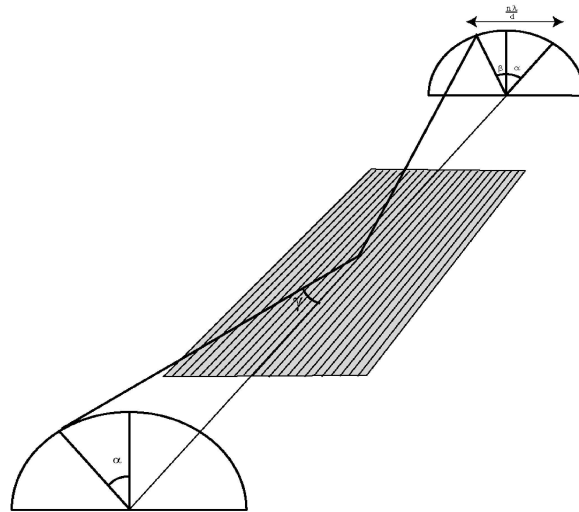


Figure 3. Off-plane grating geometry. Incident and diffracted rays are shown for the off-plane grating. The incident and diffracted rays each follow the surface of a cone of half-angle γ . The azimuthal angle α describes the incident ray as well as the zeroth order (reflected) ray. The diffracted ray is shown at angle β . Note the radial grating bars. (Taken from McEntaffer et al. 2003).

In addition to the in-plane grating, an alternative grating configuration⁸ is under study. In this configuration, the incident X-rays are quasi-parallel to the grating lines, as illustrated in Figure 3. The diffracted ray is rotated about the groove axis (effectively following the surface of a cone), so that the diffraction pattern forms an arc at the detector plane (see equation (A3)). This “conical diffraction” configuration is called the “off-plane grating” (OPG). Preliminary design parameters are also given in Table 1. Off-plane incidence and zeroth order angles may be parametrized by the cone half-angle, γ , and the azimuthal angle α of the incident ray.

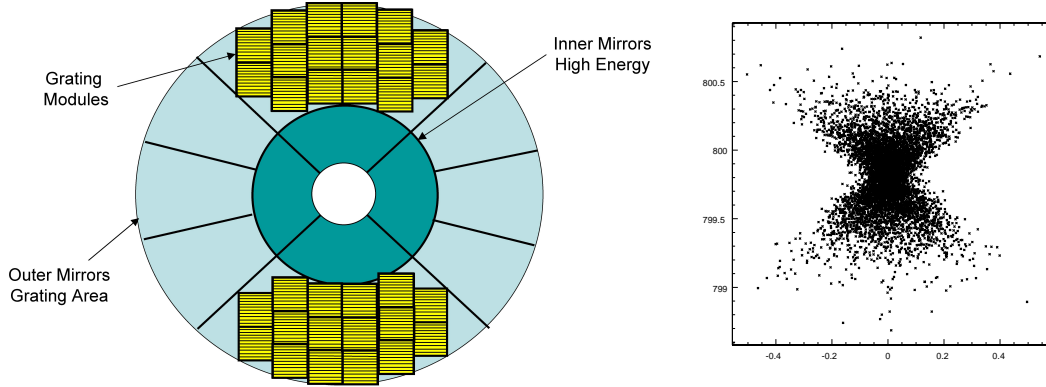


Figure 4. (Left) The OPG configuration employs *subaperturing*, in which subregions behind the optic are populated with gratings. These regions, located at the top and bottom of the SXT in this figure, result in an effective PSF that is narrowed in the dispersion direction (horizontal in the figure). This is illustrated *right* by our raytrace of the zeroth order image formed under subaperturing. Note the bowtie shape and the substantially narrowed distribution in the dispersion direction.

2. THE OFF-PLANE GRATING AND SPECTRAL RESOLUTION

The off-plane grating configuration holds several potential advantages over the in-plane configuration. Reflectivity from the gold grating surface will be higher for small grazing angles than for larger ones. Since conical diffraction strictly limits the angle of the diffracted ray with respect to the grating surface, higher reflection efficiencies may be obtained in the OPG. Moreover, groove illumination is better, with less shadowing,⁹ for an off-plane grating.

In the IPG configuration, as the diffraction angle increases, the angle between the diffracted ray and the surface of the grating increases. This means that gratings must be stacked sufficiently far apart to permit adequate diffraction range. The OPG, however, allows its full diffraction range within a strictly confined cone angle, so that packing density can be improved.

The advantages of increased grating efficiency and packing density with the OPG design imply that a smaller region of the SXT can be covered while maintaining the same RGS effective area. Stopping down the aperture in the dispersion direction will limit the spot size in the dispersion direction, increasing spectral resolution proportionately. This is illustrated in Figure 4, where only sub-regions at the top and bottom of the SXT are populated. The impact of this technique of *subaperturing* is illustrated by the raytraced zeroth order image to the right in Figure 4, which clearly shows a bowtie shape narrowed at the center.

Further increases in spectral resolution are possible if the dispersed contributions from each module are not superimposed on each other, but are instead spread out by reorienting the modules. This is illustrated in Figure 5: the zeroth order image, formed of reflected rays from multiple modules, forms a bowtie shape. The dispersed rays, however, are directed slightly differently from each module, forming a crescent shape. In such a case, the effective width in the dispersion direction is reduced to little more than the contribution from a single module.

The impact of each of these steps to improve spectral resolving power is illustrated in Figure 6. (This figure is illustrative only, and not intended to be numerically correct.) Moving counter-clockwise from the bottom, the lowest resolving power is found for off-plane gratings fully populating the outer annulus of the SXT aperture. The second curve shows that subaperturing achieves close to a factor of two improvement. The next (dashed) curve approximates the in-plane grating fully populating the SXT. The highest resolution curve illustrates the OPG with both subaperturing *and* reorienting the modules to form a crescent-shaped or scalloped dispersed image. This paper reports the results of raytrace modeling the OPG for this final case, and gives numerical estimates for the resolving power that may be expected from such an arrangement.

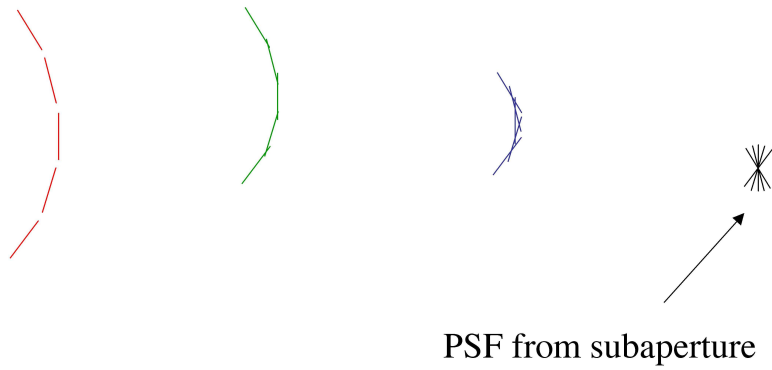


Figure 5. Spectral resolving power can be increased by reorienting modules so that the dispersed rays from each do not overlap. The resultant dispersed image is crescent-shaped, and the width in the dispersion direction is effectively reduced to the contribution from a single module.

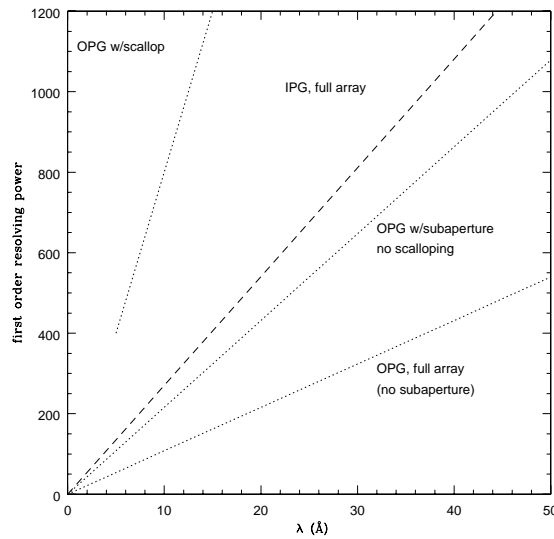


Figure 6. Representative resolving powers to be expected from four configurations (for illustrative purposes only). The bottom curve is for the OPG fully populating the region behind the outer annulus of the SXT. The next curve up is for the OPG with subaperturing. The third (dashed) curve represents the IPG fully populating the aperture behind the outer annulus. The highest curve represents a subaperture arrangement of the OPG, with individual modules oriented so as to form a crescent shaped or scalloped dispersed image.

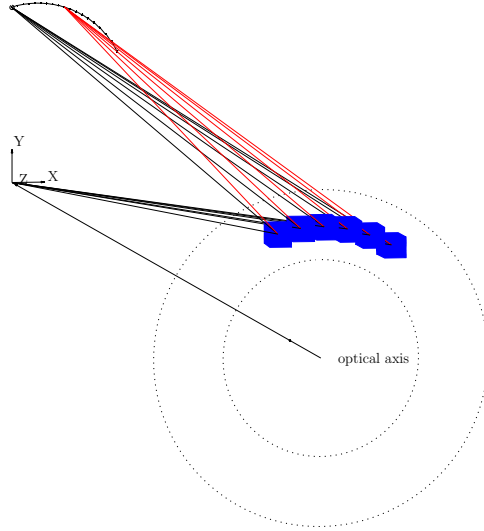


Figure 7. Layout assumed for the raytrace modeling. The grating modules are arrayed in a plane perpendicular to the optical axis that is located at a distance 8988 mm from the telescope focus. Rays that are not intercepted by the gratings converge to the telescope focus at the coordinate origin (0,0,0). Rays are reflected from the gratings to the zeroth order, which was captured by the detector at (0, 799.8, -17.79). (Note that the detector plane was set back behind the SXT focus, being placed ~ 18 mm farther from the optic.) Rays are dispersed (along $+x$) following the diffraction arc. The grating modules were arrayed at a fixed distance (600mm) from the optical axis.

3. MODELING THE SPECTRAL RESOLUTION

3.1. RAYTRACE SIMULATIONS

The raytrace software consists of about 1000 lines of code written in the S-Lang (<http://www.s-lang.org/>) scripting language and interpreted by the ISIS¹⁰ spectral modeling program.

A right-handed coordinate system for the simulations was defined with the imaging focus at the origin, with the positive z axis along the optical axis towards the SXT, the positive y axis in the vertical direction, and the positive x axis to the right as viewed from the SXT (see figure 7).

The simulations of the off-plane gratings assumed seven identical grating modules, each containing ten identical 100mm \times 100mm gratings such that any one grating module is interchangeable with another. The gratings themselves were constructed via the replication of a single reference grating with a period of 1724Å (5800 lines/mm). The geometric parameters controlling the simulation consisted of the location of the center of the reference grating with respect to the optical axis, the incidence angle ψ_i of the X-ray light at the reference position with respect to the grating surface, and the distance to zeroth order from the imaging focus. For the simulations presented here, the zeroth order was assumed to lie in the yz plane 800 mm from the focus, the incidence angle ψ_i was taken to be 2.545° , and the center of the reference grating was assumed to be 600 mm above the optical axis in the yz plane (i.e., at $x=0, y=+600$). The so-called “hub-angle” or azimuthal incidence angle α was fixed at 30° .

With the above parameters specified, the rest of the geometry was readily determined. In particular, the position of zeroth order was found to be at (0, 799.8, -17.79), and the position of the reference grating at (0, 600, 8988). The local groove direction \hat{l} at the center of the grating followed from the constraint on the hub angle. The grooves themselves were assumed to be radial with a radius R of 9020 mm (see the appendix for details).

A reference module was constructed by stacking 10 copies of the reference grating 10 mm above one another. The center of the reference module was moved to the reference position and each grating in the module was individually pivoted about its center to a position such that incoming rays would be reflected in the direction of

zeroth order. This “fanning” prescription was used to guarantee a tight zeroth order PSF. The only other degree of freedom left to determine for an individual grating was a rotation about the grating’s normal. This angle was determined by the constraint that each grating in the module produce a dispersion curve that intersected the others at the top of the dispersion circle.

The rest of the modules were created from a copy of the reference module and then translated to a position with the same z coordinate as the reference module but positioned to be the same distance from the optical axis. Thus, all the modules were placed in a single plane. The final positions of the 7 modules for the top half of the SXT are shown in Figure 7. Each of the modules was individually oriented such that the grating at the center of each module would have the same zeroth order position as previously determined. This prescription left only one other degree of freedom per module to be determined: the rotation angle about the normal to the central grating. The final rotation for each module was fixed by demanding that the dispersion curve generated by the module pass through a specified point. A different point was chosen for each module in order to obtain high spectral resolution. This positioning algorithm, together with “sub-aperturing” described below, is what gives rise to the crescent-shaped line profiles of Figures 8 and 9.

The simulation did not include an actual ray-trace model for the SXT. Rather, the expected effects of the SXT were modeled as follows. Each ray intercepting a grating was generated by randomly choosing a point on one of the 70 gratings. The ray was given an initial direction pointing to the imaging focus as one would have for a perfect optic. In this scenario the initial ray lies in a plane that contains the optical axis and the position of the ray. The ray was “blurred” in a two-stage process. First, the ray’s direction was changed by rotating the ray about the axis normal to the plane and passing through the position of the ray by an angle drawn from a gaussian distribution with a specified FWHM. For this “tangential” blur, a value of 15 arc-sec was used. Second, the ray was given a “sagittal” blur by rotating it about the axis lying in the plane and normal to the (stage-1) direction of the ray by a gaussian-distributed angle with a FWHM of 1.6 arc-sec. The much smaller FWHM for the out-of-plane blur was assumed to mimic the sub-aperturing effect.

The ray was subsequently diffracted using equation (A1) and projected to the detector plane where its position was measured. The raytrace utilized a single detector plane parallel to the xy plane but located at the zeroth order position $z = -17.79$. This position gives the tightest zeroth order PSF. In the future, other positions will be explored in order to further increase the spectral resolution.

3.2. RAYTRACE ANALYSIS

One of the advantages of using simulated data is that the wavelengths of the detected events can be precisely known. One does not have such a luxury when dealing with real data. Instead the pipeline processing software will have to assign wavelengths to events based upon the relevant calibration data. A small challenge presented by the crescent-shaped line profiles produced by the off-plane gratings will involve the transformation of CCD pixel coordinates of the events to dispersion and cross-dispersion coordinates. The subsequent data analysis is facilitated in such a coordinate system where wavelengths may be readily assigned and events binned into spectra.

To measure the resolution of the grating modules for the simulations of the off-plane gratings, we proceeded in a similar manner. To this end, a series of “calibration-runs” was performed by using the simulator to generate a number of diffracted PSF profiles at various wavelengths. For each wavelength λ_i ISIS was used to fit a parabola of the form

$$x = A_i + B_i(y - C_i)^2 \tag{1}$$

to the event coordinates with A_i , B_i , and C_i allowed to vary. Then each set of parameters was fit as a function of λ . In particular, the following functional forms were used:

$$\begin{aligned} A(\lambda) &= a_0 + a_1\lambda + a_2\lambda^2, \\ B(\lambda) &= \frac{b_0\lambda}{1 + b_1\lambda^{b_2}}. \end{aligned} \tag{2}$$

The choice for the functional form for $C(\lambda)$ was motivated by the fact that the intersection of a plane with a cone is represented by a conic. In this case, a rotated ellipse was chosen to represent $C(\lambda)$. As such, $C(\lambda)$

was characterized by five parameters: the position of the ellipse in the detector plane, the major and minor axes, and the rotation angle. The exact functional form of $C(\lambda)$ is left as a simple exercise for the reader. The cross-dispersion coordinate η was represented simply as

$$\eta = y - C(\lambda) \quad (3)$$

The above parameterization gives the (x, y) detector coordinates as explicit functions of the dispersion and cross-dispersion coordinates (λ, η) , i.e.,

$$\begin{aligned} x &= x(\lambda, \eta) \\ y &= y(\lambda, \eta). \end{aligned} \quad (4)$$

While this permits an easy transformation from (λ, η) to (x, y) , the equations must be inverted numerically to determine (λ, η) from (x, y) .

To determine the resolving power of the off-plane grating array, the above technique was used to assign a wavelength and cross-dispersion coordinate to each of the diffracted events. The effect of this procedure is shown in the scatter plots of λ versus η in Figures 8 and 9. The resulting data were then binned into a spectrum using the S-Lang histogram functions and then fitted to a one-dimensional gaussian profile by ISIS. From the width of the gaussian, the resolving power was readily characterized.

4. RAYTRACE RESULTS

Figure 8 illustrates the raytrace results for four wavelengths sampling the RGS range: 10 Å, 25 Å, 40 Å and 60 Å. For each case, three plots are given:

the raw raytrace in detector coordinates of the first order for two monochromatic lines separated by 0.028 Å. This particular choice was made to mimic McEntaffer *et al.*, 2003 in order to facilitate direct comparison.

the raytrace in dispersion - cross dispersion coordinates (λ, η) ,

the dispersion histogram (or spectrum). Gaussians fitted to the histograms for these X-ray lines provided a best-fit width σ , from which we obtained the full-width-at-half-maximum (FWHM=2.354 σ) or the half-energy width (=1.349 σ).

For each of the raytrace plots of Figure 8, seven modules were arrayed behind the top part of the SXT as shown in Figure 7. The gratings were assumed to have a size of 100mm×100mm (to facilitate comparison with McEntaffer *et al.*, 2003), and the optic was modeled to approximate a realistic Constellation-X type optic.

In order to assess the impact of optic quality, grating size and grating placement on the spectral resolution, additional raytrace modeling was performed assuming:

100mm×100mm gratings, assuming a *perfect* optic,

100mm×200mm gratings, and

100mm×100mm gratings arrayed in modules behind the *bottom* of the SXT.

The results of this modeling are shown in Figure 9.

Numerical assessment of these results is expressed as spectral resolving power in Figure 10. The plot at the left of Figure 10 indicates the resolving power, $\lambda/\delta\lambda$, where $\delta\lambda$ is interpreted as either the measure in FWHM or half-energy width. (The wavelength axis gives $m\lambda$, where m is the order. First order resolving powers are read directly from the plot.) The numerical difference between these two definitions for resolving power is a factor of 1.7 with no difference whatsoever in the actual quality of performance, so care must be taken to define clearly what is meant. This plot also shows the degradation that occurs when the grating size is enlarged from 100 mm length to 200 mm length.

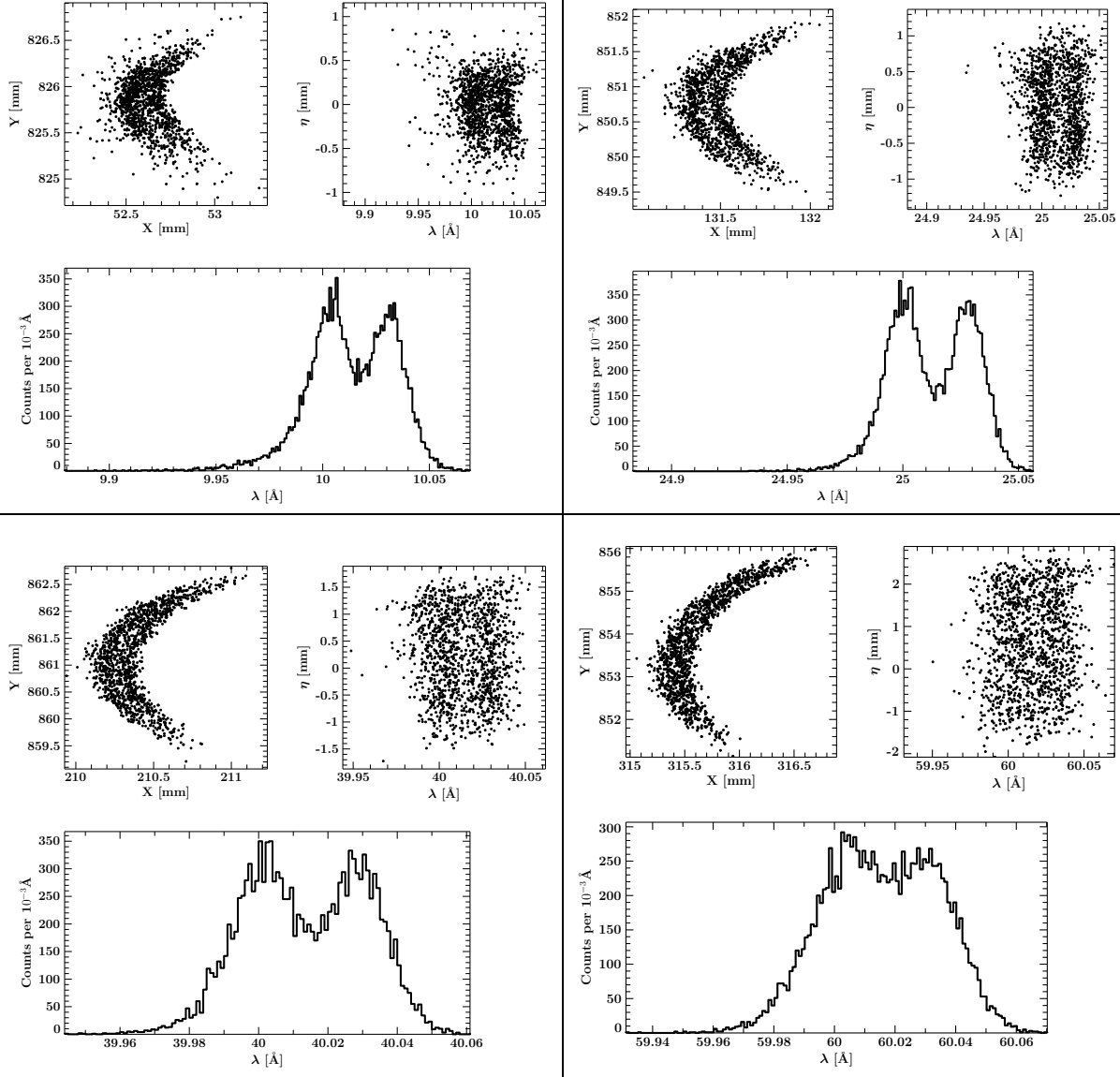


Figure 8. Raytraces at four wavelengths: 10 Å, 25 Å, 40 Å and 60 Å. Each of the four sets of plots illustrates the raw raytrace in detector coordinates of two monochromatic X-ray lines (λ and $\lambda+0.028$ Å) in first order, the distribution in the dispersion and cross dispersion coordinates, and the histograms along the dispersion axis. Each raytrace contains 7 modules arrayed behind the top part of the optic, and assumes a realistic PSF. Each grating is assumed to have 100mm \times 100mm size.

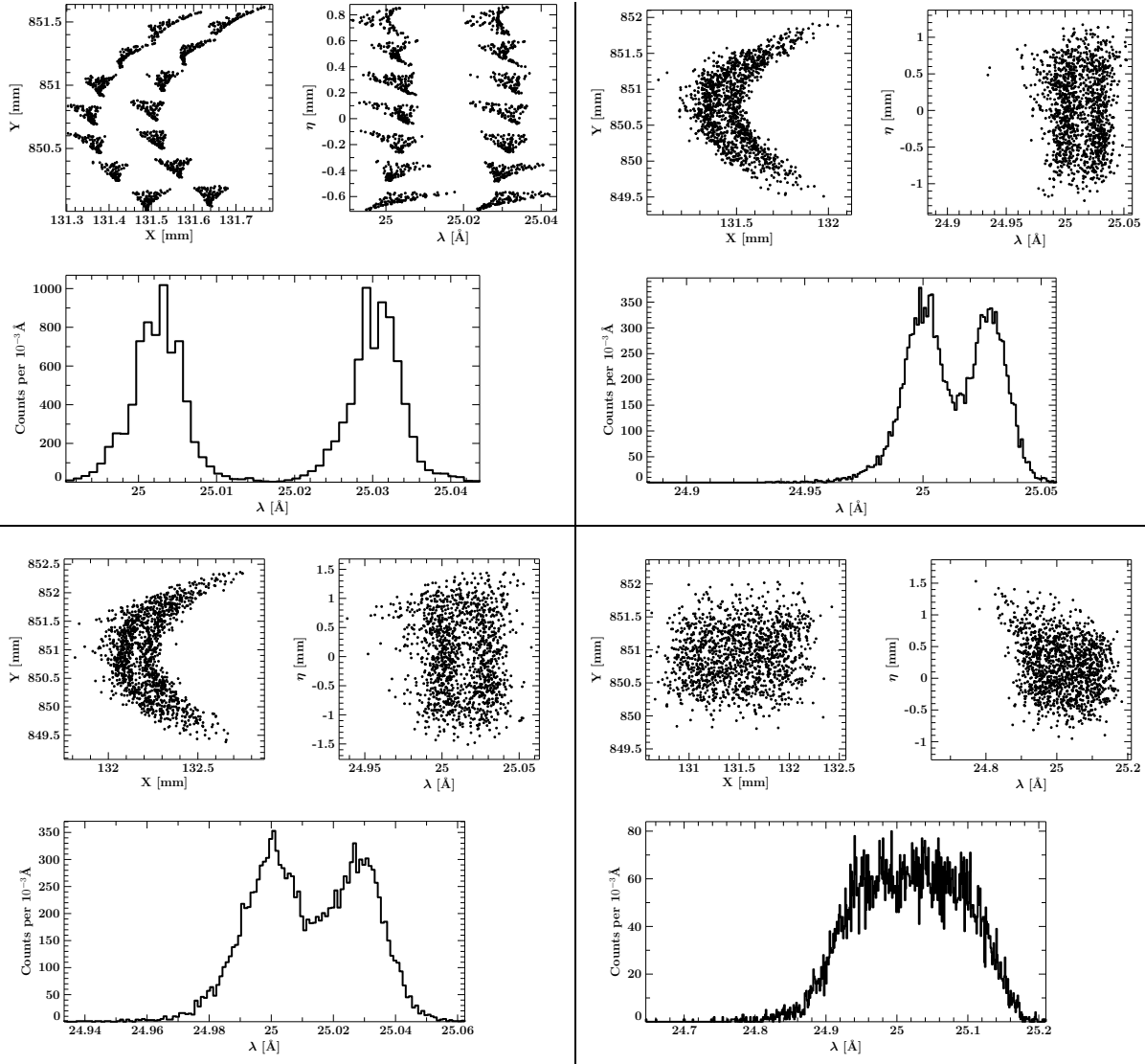


Figure 9. Relative impact of the optic quality, grating size, and module placement. Each of the four sets of plots illustrates the raw raytrace in detector coordinates of two monochromatic X-ray lines (25.0Å and 25.028Å) in first order, the distribution in the dispersion and cross dispersion coordinates, and the histograms along the dispersion axis. The first set (upper left) is a raytrace of 7 modules arrayed at the top part of the optic, assuming a *perfect* optic. Each grating is modeled to have 100mm×100mm size. The second set of raytrace figures (upper right), employs the same module geometry and placement, but assumes a realistic Constellation-X type optic. The third set (lower left), has the same assumptions, except the grating size is increased to 100mm×200mm. In the fourth set (lower right), 100mm×100mm gratings are modeled with a realistic optic, but the grating modules are placed behind the *lower or bottom* section of the optic without changing the focal plane. Each of these four steps successively degrades the spectral resolution.

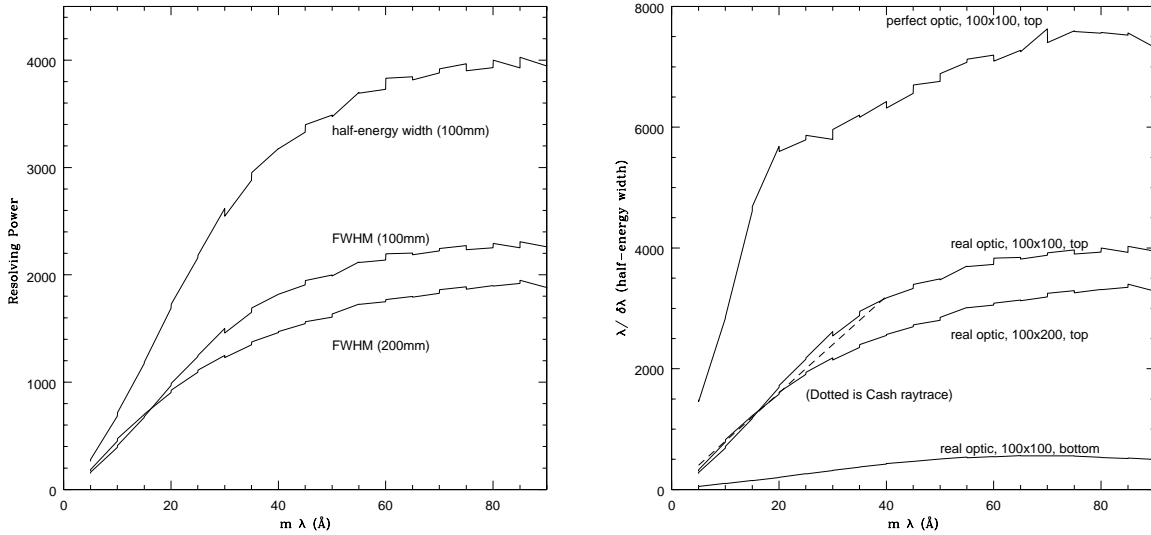


Figure 10. (Left) Resolving power defined using two interpretations for $\delta\lambda$: FWHM, or half-energy width. The numerical difference is approximately a factor of 1.7. (Right) The impact of optic quality, grating size and placement of grating modules on resolving power. Gratings arrayed at the bottom of the SXT optic suffer a “defocus effect” due to severe path length differences.

The plot at the right of Figure 10 indicates the degradation, in order, from perfect optic, to real optic, to larger grating size, to placement of grating modules at the bottom of the SXT. Also indicated in the figure (dashed line) is the result of raytraces by Cash (private communication). This curve is expected to be representative near 35 \AA (Cash’s blaze); the linearity may fall somewhat outside this range, so it has only been plotted to 40 \AA . Agreement with our raytrace (for $100\text{mm}\times 100\text{mm}$ gratings arrayed in the top of the SXT) appears to be excellent.

Each of the successive downward steps in resolving power is expected as the optic quality is lessened and the grating size is increased, but the result encountered with module placement at the bottom of the SXT deserves special comment. Examination of Figure 7 indicates that path lengths from the gratings at the top of the SXT to the optic focus are approximately equal to the path lengths from the gratings to the nominal zeroth order and dispersion arc locations on the detector plane. This is in stark contrast to the situation for gratings at the *bottom* of the SXT: the path length to the chosen zeroth order location is much longer than the path length to the optic focus. This “defocus effect” severely degrades the resolution. Any arraying prescription that optimizes performance for gratings at the top half of the SXT is expected to be unsuitable for gratings at the bottom of the SXT.

5. SUPPORTING MODELING EFFORTS

Modeling at Ball Aerospace: Among our co-authors, the modeling group at Ball Aerospace and Technologies Corporation set up a simplified model of the proposed Constellation-X SXT off-plane RGS to optimize grating design parameters and to study spectrometer performance. The model used a sequential ray-trace package called Zemax which has been validated for grazing-angle reflection telescopes commonly used in X-ray optics. Instead of fully populating all of the SXT mirror shell segments and RGS gratings, this model selectively incorporated representative shell/gratings to sample various combinations of telescope and grating orientations. The maximum numbers used were 54 shell segments and 18 gratings (3 segments feeding into each grating) covering the proposed grating array. By limiting the number of optics in the model, a large grating parameter space could be explored quickly to ensure a global optimization. However, by excluding the majority of gratings, the sampled subset may

not yield realistic spectrometer spot diagrams. The Ball co-authors compared the spot diagrams from Zemax with those from a complete model made using the non-sequential ASAP package. After adjusting the number and position of shell/gratings, they concluded that the Zemax model produced similar results to the ASAP model.

They performed a preliminary optimization of holographic grating design at 5000 l/mm assuming a single grating type throughout the entire spectrometer. The derived parameters agree with previous results⁹ obtained through independent techniques. The model showed that there is an optical path-length difference between gratings located on azimuthally opposite sides of the mirror assembly, causing defocus of the spectral lines. With only one half of the array, resolving powers well over 1000 can be seen in the first-order spectrum. With both halves, however, the resolving power degrades to 200-300. In the future, this model can be utilized to further optimize the grating design taking into account the influence of typical telescope and grating errors due to fabrication, mounting, and alignment. To correct for the defocus effect, it is possible to examine various configurations using two grating types in the spectrometer. Some of the gratings would be designed to have a weak focusing power in order to compensate for optical path-length difference and achieve the best resolving power.

Modeling at Columbia University: To check the independent OPG array raytrace results reported here, the raytrace package described by Rasmussen et al. (2003) was modified to reflect the current layout. The number of modules was reduced to six containing 20 gratings each, located behind the top part of the optic. The arraying prescription was modified, and the location of the detector plane was moved back to approximate the current simulations. With these adaptations, the raytrace confirmed that the resolving powers seen in Figure 10 above could be achieved.

Modeling at Smithsonian Astrophysical Observatory: Among our co-authors, the modeling group at Smithsonian Astrophysical Observatory (SAO) has taken on the task of extending its software suite SAOsac¹¹ to include reflection gratings for both IPG and OPG configurations. This suite was developed as part of SAO’s work on the Chandra X-Ray Observatory, and models grazing incidence optics as well as transmission gratings. The optics models are immediately applicable to the Con-X Optics, and the grating model has now been extended to handle IPG and OPG configurations. Although fully arrayed raytraces have not yet been performed, SAOsac will be useful in assessing the relative merits of the two grating configurations. SAOsac simulates the geometric propagation of rays through models of the components in the optical system. It is designed as an engineering tool, to perform trade and sensitivity studies and to characterize system performance. It can incorporate as-built hardware specifications, permitting high fidelity simulations of the actual optical system.

6. CONCLUSIONS

The raytrace modeling presented here did not optimize module placement for “best” resolution, and did not include a fully populated sub-aperture arrangement. Nevertheless, preliminary analysis suggests that first order resolving powers over 1000 (defined by half-energy width) are achievable for sufficiently long wavelengths ($\lambda \gtrsim 12\text{\AA}$. For shorter wavelengths, higher orders are needed.) Cross-comparison with other raytraces (Cash, Rasmussen, Gallagher and Huang) employing similar arrangements shows reasonable agreement with the results presented here.

An important finding is that separate accommodation must be made for gratings at the bottom of the SXT (i.e., the subaperture zone that is far from the zeroth order). This might include a separate diffraction arc with a separate readout detector, curved gratings to achieve a focusing effect, a modified optic, or some other scheme. It should be noted that a raytrace for the full array of modules remains to be done, with realistic effective areas included. Complete assessment of the grating configuration will take into account increased background (since the dispersed line is spread over a larger detector area). Finally, we note that pipeline processing (extracting dispersion coordinates) is not straightforward, and only the first steps have been taken here.

APPENDIX A. THE RADIAL GROOVE PRESCRIPTION

The purpose of this section is to derive an expression for the hub distance for the radial gratings modeled by simulations described in section 3.1. Although an equation describing an additional period gradient or “chirp” is also obtained, such gratings were not used in this work.

The diffraction equation may be written in the compact form

$$\hat{n} \times (\hat{p}' - \hat{p}) = \frac{m\lambda}{d} \hat{l}, \quad (\text{A1})$$

where \hat{p} represents the direction of an incoming photon (before diffraction) with wavelength λ , and \hat{p}' denotes the direction of the diffracted ray into order m . The vector \hat{n} is normal to the plane of the grating, and \hat{l} is a vector specifying the local groove direction. The period of the grating is denoted by d . A local orthonormal right-handed coordinate basis may be constructed from the triad of unit vectors $(\hat{d}, \hat{l}, \hat{n})$, where $\hat{d} = \hat{l} \times \hat{n}$.

It is easy to see that this formalism gives rise to so-called ‘‘conical-diffraction’’ by considering how the direction \hat{p}' of the diffracted ray changes as the wavelength λ changes. It trivially follows from equation (A1) that

$$\hat{n} \times \delta\hat{p}' = \frac{m\delta\lambda}{d} \hat{l}, \quad (\text{A2})$$

and from this

$$\delta\hat{p}' \cdot \hat{l} = 0. \quad (\text{A3})$$

In other words, the change in the diffracted ray will be such that its component along the groove direction \hat{l} does not change. Hence, the change in the diffracted direction \hat{p}' may be described as a rotation about the \hat{l} axis. This describes canonical diffraction.

Equation (A1) may be put into more familiar forms by taking cross-products of it with \hat{l} and \hat{d} to produce

$$(\hat{p}' - \hat{p}) \cdot \hat{l} = 0 \quad (\text{A4})$$

and

$$(\hat{p}' - \hat{p}) \cdot \hat{d} = \frac{m\lambda}{d}, \quad (\text{A5})$$

respectively.

For maximum resolution, it is required that the diffracted rays meet at the same point \vec{S} in space for some fixed wavelength λ . This constraint may be expressed by

$$\vec{S} = \vec{x} + \hat{p}'(\vec{x})|\vec{S} - \vec{x}| \quad (\text{A6})$$

where \vec{x} is an arbitrary point on the grating surface. Generally speaking, the only way for this constraint to be satisfied for any point \vec{x} is for the local grating geometry to vary as a function of \vec{x} . That is, the local basis vectors \hat{n} , \hat{l} , and \hat{d} , as well as the period d vary with position. The goal of the following is to characterize this dependence. To this end, assume that the incoming rays $\hat{p}(\vec{x})$ are directed towards the imaging focus \vec{F} , i.e.,

$$\hat{p}(\vec{x}) = \frac{\vec{F} - \vec{x}}{|\vec{F} - \vec{x}|} \quad (\text{A7})$$

Varying equation (A1) with respect to \vec{x} yields

$$\hat{n} \times (\delta\hat{p}' - \delta\hat{p}) = \frac{m\lambda}{d} \delta\hat{l} - \frac{m\lambda}{d^2} (\delta d) \hat{l}, \quad (\text{A8})$$

where

$$\delta\hat{p}' = \frac{-\delta\vec{x}}{|\vec{S} - \vec{x}|} + \frac{\hat{p}'}{|\vec{S} - \vec{x}|} (\hat{p}' \cdot \delta\vec{x}) \quad (\text{A9})$$

and

$$\delta\hat{p} = \frac{-\delta\vec{x}}{|\vec{F} - \vec{x}|} + \frac{\hat{p}}{|\vec{F} - \vec{x}|} (\hat{p} \cdot \delta\vec{x}) \quad (\text{A10})$$

follow from equations (A6) and (A7).

Now let A be defined as the average of $|\vec{S} - \vec{x}|$ and $|\vec{F} - \vec{x}|$, and ΔA be their difference, i.e.,

$$\begin{aligned} |\vec{S} - \vec{x}| &= A + \Delta A/2 \\ |\vec{F} - \vec{x}| &= A - \Delta A/2 \end{aligned} \quad (\text{A11})$$

From these definitions and equation (A1) it is straightforward to show that

$$\delta\hat{p}' - \delta\hat{p} = \frac{\hat{p}'}{A}(\hat{p}' \cdot \delta\vec{x}) - \frac{\hat{p}}{A}(\hat{p} \cdot \delta\vec{x}) + O\left(\frac{\Delta A}{A}\right) \quad (\text{A12})$$

and

$$\hat{n} \times (\delta\hat{p}' - \delta\hat{p}) = \frac{\hat{n} \times \hat{p}'}{A}(\hat{p}' - \hat{p}) \cdot \delta\vec{x} + \hat{l}\left(\frac{m\lambda}{d}\right)\frac{(\hat{p}' \cdot \delta\vec{x})}{A} + O\left(\frac{\Delta A}{A}\right). \quad (\text{A13})$$

Substituting the above result into equation (A8) yields

$$0 = \left[\frac{\hat{n} \times \hat{p}'}{A}(\hat{p}' - \hat{p}) \cdot \delta\vec{x} - \frac{m\lambda}{d}\delta\hat{l} \right] + \hat{l}\left(\frac{m\lambda}{d}\right)\left[\frac{(\hat{p}' \cdot \delta\vec{x})}{A} + \frac{\delta d}{d} \right] + O\left(\frac{\Delta A}{A}\right). \quad (\text{A14})$$

Equation A14 may be simplified by considering variations along the directions \hat{l} and \hat{d} separately. First consider the effect of variations along \hat{l} , i.e.,

$$\delta\vec{x} = (\delta x)\hat{l}. \quad (\text{A15})$$

Substituting this form of $\delta\vec{x}$ into equation (A14) and using equation (A4) followed by the dot product with \hat{l} produces

$$\frac{\delta d}{\delta x} = -\frac{d}{A}(\hat{p} \cdot \hat{l}) + O\left(\frac{\Delta A}{A}\right). \quad (\text{A16})$$

This equation gives the form of the period gradient with respect to variations along the groove direction. By dotting with \hat{d} instead of \hat{l} one obtains

$$0 = \frac{\delta\hat{l}}{\delta x} + O\left(\frac{\Delta A}{A}\right), \quad (\text{A17})$$

i.e., that to first order the groove direction remains constant with respect to variations along it.

Now consider variations along the \hat{d} direction of with

$$\delta\vec{x} = (\delta x)\hat{d}. \quad (\text{A18})$$

Using similar similar manipulations as above one can show that

$$\frac{\delta\hat{l}}{\delta x} = -\frac{\hat{p} \cdot \hat{l}}{A}\hat{d} + O\left(\frac{\Delta A}{A}\right) \quad (\text{A19})$$

and

$$\frac{\delta d}{\delta x} = -\frac{d}{A}\left[2\hat{p} \cdot \hat{d} + \frac{m\lambda}{d}\right] + O\left(\frac{\Delta A}{A}\right). \quad (\text{A20})$$

It is easy to see that equations (A16) and (A19) may be interpreted as describing a diffraction grating with radial grooves directed towards a common center. The fact that equation (A16) indicates that the period decreases as one moves along the groove is consistent with an increase in the groove density towards the center. Moreover, equation (A19) says that the groove direction changes as one moves in the transverse direction from groove to groove. Both these equations are consistent with radial grooves whose center or hub is located at a distance $R = A/\hat{p} \cdot \hat{l}$ from the grating.

Equation A20 indicates that the period of the grating should decrease as one moves in the direction transverse to the grooves. Such a grating is said to have a ‘‘chirp’’.

ACKNOWLEDGMENTS

The authors would like to thank Eric Fischbach for assistance with rotation matrices and solutions to higher order equations. We also thank Stephen S. Murray for providing invaluable assistance with image analysis and fitting. We thank Timo Saha and Dave Content for their support and assistance. This work was supported by NASA through contract NAS8-01129 and by the Smithsonian Astrophysical Observatory (SAO) contract SV3-73016 for the Chandra X-ray Center (CXC). It is also supported under NASA grants NAG5-12583, NAG5-13217 and NNG04GB16G.

REFERENCES

1. N. E. White and H. D. Tananbaum, “Constellation-X mission: science objectives and implementation plan,” in *X-Ray and Gamma-Ray Telescopes and Instruments for Astronomy. Edited by Joachim E. Truemper, Harvey D. Tananbaum. Proceedings of the SPIE, Volume 4851, pp. 293-303 (2003).*, pp. 293–303, Mar. 2003.
2. N. White and A. Diaz, “NASA s Beyond Einstein Programme: From the Big Bang to Black Holes,” in *COSPAR, Plenary Meeting*, 2004.
3. R. L. Kelley, “The X-Ray Microcalorimeter Spectrometer for the Constellation-X Mission,” *AAS/High Energy Astrophysics Division* **35**, pp. –+, Mar. 2003.
4. R. Petre, W. W. Zhang, D. A. Content, T. T. Saha, J. Stewart, J. H. Hair, D. Nguyen, W. A. Podgorski, W. R. Davis, M. D. Freeman, L. M. Cohen, M. L. Schattenburg, R. K. Heilmann, Y. Sun, and C. R. Forest, “Constellation-X spectroscopy X-ray telescope (SXT),” in *X-Ray and Gamma-Ray Telescopes and Instruments for Astronomy. Edited by Joachim E. Truemper, Harvey D. Tananbaum. Proceedings of the SPIE, Volume 4851, pp. 433-440 (2003).*, pp. 433–440, Mar. 2003.
5. C. J. Hailey, F. E. Christensen, W. W. Craig, F. A. Harrison, J. Koglin, R. Petre, D. L. Windt, and W. W. Zhang, “Overview of segmented glass optics development for the Constellation-X hard X-ray telescope,” in *X-Ray and Gamma-Ray Telescopes and Instruments for Astronomy. Edited by Joachim E. Truemper, Harvey D. Tananbaum. Proceedings of the SPIE, Volume 4851, pp. 519-527 (2003).*, pp. 519–527, Mar. 2003.
6. G. R. Ricker, M. Bautz, J. Doty, K. G. Flanagan, s. Kissel, G. Prigozhin, and M. Schattenburg, “Reflection grating spectrometer focal plane camera (RFC) for the Constellation-X Mission,” in *High-Energy Detectors in Astronomy. Edited by Holland, Andrew; Struder, Lothar. Proceedings of the SPIE, Volume 5501 (2004).*, June 2004.
7. S. M. Kahn, F. B. Paerels, J. R. Peterson, A. P. Rasmussen, M. L. Schattenburg, G. R. Ricker, M. W. Bautz, J. P. Doty, G. Y. Prigozhin, J. A. Nousek, D. N. Burrows, J. E. Hill, and W. C. Cash, “Large-area reflection grating spectrometer for the Constellation-X mission,” in *Proc. SPIE Vol. 3765, p. 94-103, EUV, X-Ray, and Gamma-Ray Instrumentation for Astronomy X, Oswald H. Siegmund; Kathryn A. Flanagan; Eds.*, pp. 94–103, Oct. 1999.
8. W. C. Cash, “X-ray optics. II - A technique for high resolution spectroscopy,” *Applied Optics* **30**, pp. 1749–1759, May 1991.
9. R. L. McEntaffer, W. C. Cash, and A. F. Shipley, “Off-plane gratings for Constellation-X,” in *X-Ray and Gamma-Ray Telescopes and Instruments for Astronomy. Edited by Joachim E. Truemper, Harvey D. Tananbaum. Proceedings of the SPIE, Volume 4851, pp. 549-556 (2003).*, pp. 549–556, Mar. 2003.
10. J. C. Houck and L. A. Denicola, “ISIS: An Interactive Spectral Interpretation System for High Resolution X-Ray Spectroscopy,” in *ASP Conf. Ser. 216: Astronomical Data Analysis Software and Systems IX*, pp. 591–+, 2000.
11. D. H. Jerius, L. Cohen, R. J. Edgar, M. Freeman, T. J. Gaetz, J. P. Hughes, D. Nguyen, W. A. Podgorski, M. Tibbetts, L. P. Van Speybroeck, and P. Zhao, “The role of modeling in the calibration of the Chandra’s optics,” in *X-Ray and Gamma-Ray Instrumentation for Astronomy XIII. Edited by Flanagan, Kathryn A.; Siegmund, Oswald H. W. Proceedings of the SPIE, Volume 5165, pp. 402-410 (2004).*, pp. 402–410, Feb. 2004.